Impact of the Mechanical Stress on Switching Characteristics of Electrochemical Resistive Memory

By *S. Ambrogio, S. Balatti, S. Choi, and D. Ielmini**

Resistive switching in oxides and other insulating materials provides a promising approach to nanoscale memory devices, where the stored logic state can be changed by activating/deactivating a conductive filament (CF).[1,2] Among resistive switching devices, the electrochemical memory (ECM) attracts strong interest because of outstanding properties such as extremely small programing current,[3] fast switching,[4] high endurance,[5] and controllable resistance states.[2,6] ECM switching is generally understood as due to metal/electrolyte charge transfer[7] and the subsequent migration of metal cations (e.g., silver),[1,2,6,8–15] however the possible impact of the mechanical stress[12,14] around the growing CF must be carefully assessed. Through switching experiments and ion-migration calculations, we provide evidence for asymmetric switching due to the different energy barriers for ion drift under positive or negative voltage. We show that the migration-barrier asymmetry can be explained by the mechanical-stress gradient opposing to CF growth and aiding its retraction during negative erase. The CF stabilization was demonstrated by properly increasing the program pulse width, which can be explained by the alleviation of the stress field through electrically-induced plastic relaxation.

Electrochemical memory (ECM), also known as programmable metallization cell (PMC) [5,6] or conductive bridge RAM,[9,15] is a semiconductor nanodevice based on the growth/dissolution of a metallic CF within a solid-state electrolyte, such as GeS_2,[7,9] GeSe,[5,6] Ag_2S,[4,10] Cu_2S,[16] AgI,[17–19] amorphous Si,[12,20] oxides[3,13,21] and even organic materials.[22] ECM have found application in non-volatile memory devices,[5,15] non-volatile switches in programmable logic,[23] nanowire logic gates[4] and artificial neural networks, where the ECM can emulate the neuron synapse thanks to its voltage-adjustable conductance.[24,25] In the ECM structure shown in **Figure 1**a, the electrolyte layer (GeS_2 in our devices) separates two electrodes, one of them consisting of a reactive metal such as Ag or Cu. Under a positive voltage applied to the reactive metal electrode, a CF is nucleated and grown (Figure 1b,c, respectively) by the migration of metallic positive ions through the electrolyte.[5] The CF is dissolved in the reset operation, where a negative voltage is applied to the top electrode to subtract conductive metal atoms from the filament. Set and reset operations under bipolar switching allow for non-volatile storage in ECM nanodevices with electrode size as small as 5 nm.[26] Whereas low-power operation[3] and fast switching[15] were demonstrated in ECMs, recent experiments on ECM devices[25,27] have questioned the long-term stability of the CF, which is necessary to enable nonvolatile storage of data. To assess the switching behavior and CF stability in ECMs, the detailed evolution of electrical, chemical and mechanical forces in the CF must be understood.

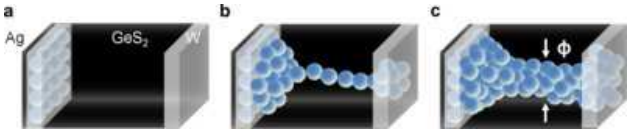

Figure 1. ECM structure and switching mechanism. a) ECM structure with Ag reactive electrode, GeS_2 electrolyte and W inert electrode. b) Nucleation of the CF through migration of cations (Ag^+) from the reactive electrode toward the inert electrode. c) Growth of the CF through further migration of cations attaching to the nucleated channel. The increase of the CF diameter φ can be model by the thermally-activated growth rate in Equation (2).

Figure 2a shows the measured current–voltage (I–V) curve for an ECM with Ag top electrode, GeS_2 electrolyte and W bottom electrode during set and reset transition. Details about the preparation of the ECM devices can be found elsewhere.[15] The set transition from high to low resistance takes place at $V_{set} \approx 0.3$ V, while the reset transition to high resistance occurs at V_{reset}. In the set process, the CF is first formed by nucleation[28,29] followed by CF growth,[6,24] which is activated by positive ion migration as shown in Figure 2b: metallic ions from the reactive-metal electrode (Ag) hop among localized states separated by energy barriers E_{A0} in amorphous GeS_2. The electric field lowers the ion-migration barrier to the value:

$$E_A = E_{A0} - \alpha q V \quad (1)$$

where $\alpha = 0.3$ is a barrier-lowering coefficient (see Figure S1 in the Supporting Information for a complete list of all model parameters used in the simulation) and V is the voltage across the electrolyte.[6,24,30] Barrier lowering enhances the hopping rate in the field direction, thus increasing the growth rate of

S. Ambrogio, S. Balatti, S. Choi, D. Ielmini, Dipartimento di Elettronica, Informazione e Bioingegneria Politecnico di Milano and IU.NET, Piazza L. da Vinci, 32 20133, Milano, MI, Italy (E-mail: daniele.ielmini@polimi.it)
Correspondence to: D. Ielmini (E-mail: daniele.ielmini@polimi.it)

the CF diameter φ according to:

$$\frac{d\phi}{dt} = A\exp - \frac{E_A}{kT} \quad (2)$$

where A is a pre-exponential constant proportional to cation mobility, T is the local temperature at the CF and E_A was obtained from Equation (1). In Equation (2), E_A controls ion migration in the vertical direction from top to bottom electrode, while the accumulation of defects along the CF causes growth in the radial direction, which is captured by the parameter φ (e.g., see Figure 1c). Note that the parameter φ represents an effective CF diameter, to properly describe non-cylindrical (e.g., conical) CF shapes and the case of multiple filaments contributing to the resistive switching.[12,26] For instance, in the case of multiple filaments the effective diameter in Equation (2) obeys $\varphi^2 = \Sigma{\varphi_i}^2$, where φ_i represents the diameter of the individual i-th filament and φ properly describes the resistance $R \propto \varphi^{-2}$ of the set state.

To control the size of the growing CF during the set transition, the current was kept equal to a compliance value $I_C = 1$ mA in Figure 2a, thus resulting in a resistance of about 0.3 kΩ in the set state. The current-controlled CF growth was explained by voltage-driven switching as follows: while the CF grows at a constant current I_C, the voltage across the CF decreases according to $V = RI_C$, where R is the decreasing resistance of the growing CF. As V decreases in Equation (1), the growth rate is quenched due to both the increasing E_A and the decreasing local temperature, as a result of the vanishing Joule heating. At the critical voltage V_C, ion migration rate becomes practically negligible with respect to the experimental timescale, thus dictating the final CF size and its resistance given by $R = V_C/I_C$.[30] The switching characteristic in Figure 2a is clearly asymmetric due to $|V_{reset}| \approx 0.15$ V being smaller than $V_C \approx 0.25$ V, which highlights that different voltages are needed to trigger ion migration in the two polarities. As a result of the asymmetric switching voltage, the switching currents in the two polarities are also different, namely the reset current I_{reset} is about half of I_C in Figure 2a.This is contrary to valence change memory (VCM) switching in oxide material systems, displaying symmetric switching with $V_C = V_{reset}$ and $I_{reset} = I_C$ for a broad range of I_C and materials.[31]

Equation (1) and (2) allow the CF size φ to be calculated during time by estimating the local temperature as:

$$T = T_0 + \frac{R_{th}}{R} V^2 \quad (3)$$

where the T_0 is the room temperature and R_{th} [KW^{-1}] is the effective thermal resistance, calculated from an analytical model for heat flow through cylindrical filament.[30] Figure 2c shows the measured and calculated I–V curves for I_C increasing between 1 nA and 100 μA. In the calculations, the voltage was swept with a rate $dV/dt = 0.75$ V s^{-1}, while the CF resistance was evaluated from $R = \rho t_{ins}/(\pi\varphi^2/4)$, where ρ is the CF resistivity and t_{ins} is the thickness of the insulating electrolyte layer (see Figure S2 in the Supporting Information). Note that E_A in Equation (1) depends on the nature of localized states capturing/emitting cations, thus different values of E_{A0} and α may be

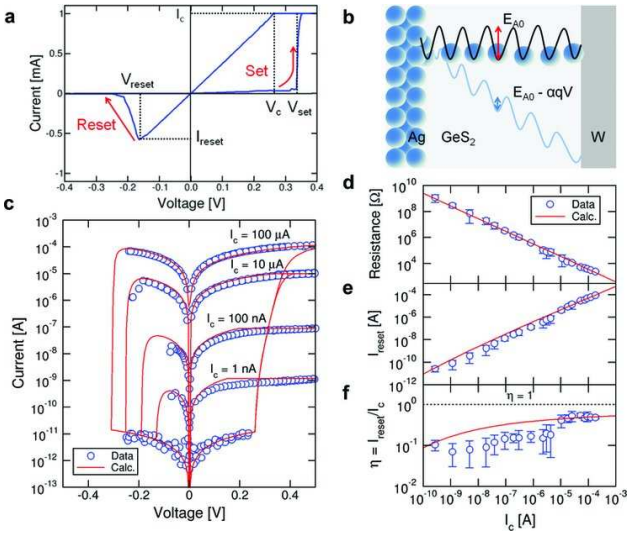

Figure 2. ECM switching characteristics and modeling. a) I–V characteristic for an ECM device showing set and reset transitions under positive and negative voltage applied to the reactive electrode. The current during the set transition was limited by a compliance current I_C = 1 mA to control the CF growth. Switching parameters V_{set}, V_{reset}, V_C and I_{reset} are defined in the figure. b) Schematic illustration of the potential energy profile for ion migration for zero or positive applied voltage. The voltage-induced barrier lowering accelerates migration in the direction of the electric field. c) Measured and calculated I–V curves for increasing I_C = 1 nA, 100 nA, 10 μA and 100 μA in a logarithmic scale. Data were obtained from an ECM device in series with a FET, used to control the maximum current I_C during the set transition. The switching asymmetry ($I_{reset} < I_C$) and the increasing V_{reset} with I_C are clearly shown. d,e,f) Measured and calculated set-state resistance R (d), I_{reset} (e) and $\eta = I_{reset}/I_C$ (f) as a function of I_C. The resistance in the set state R decreases proportionally to ${I_C}^{-1}$ due to the constant voltage V_C for the quenching of the CF growth process. The reset current I_{reset} is 10% to 50% of I_C, which is reproduced in the calculations by assuming different energy barriers for ion migration to/from the reactive electrode.

expected before and after nucleation (Figure 1a,b, respectively). Similarly, different equations might be needed to estimate R_{th} and R in the case of an incomplete CF with respect to the model of a conducting CF connecting top and bottom electrodes in Figures 1b,c. To account for the peculiarities of CF nucleation while keeping a reasonably simple model, we assumed that CF nucleation can only take place above a characteristic voltage V_{set} = 0.25 V, marking the threshold to reach the significant temperature and electric field to trigger ion migration in the initial condition of Figure 1a. Above V_{set}, CF growth was allowed to start according to Equation (1)–(3). Although φ in Equation (2) is strictly defined only for a cylindrical CF in Figure 1c, it might be viewed as an equivalent diameter for other CF geometries, such as conical shapes or incomplete CF which do not connect top and bottom electrodes yet.[30,32] Positive and negative val-

ues of A were used to describe CF growth (set) and dissolution (reset), respectively, with $|A| = 10^{-3}$ ms^{-1}.

The resistance after the set transition in Figure 2c is inversely proportional to I_C, consistently with a characteristic voltage $V_C \approx 0.25$ V marking the suppression of CF growth at constant current I_C. This behavior is confirmed by Figure 2d, where both measured and calculated results indicate a constant product $RI_C = V_C \approx 0.25$ V along a broad range of 6 decades of I_C. The switching characteristics are again visibly asymmetric with $V_{reset} < V_C$ and $I_{reset} < I_C$, as also summarized by the measured and calculated I_{reset} (Figure 2e) and I_{reset}/I_C (Figure 2f) as a function of I_C. The reset current I_{reset} increases from about $0.1I_C$ to about $0.5I_C$ for increasing current compliance, hence CF size. The increasing I_{reset}/I_C can be understood by size-dependent CF erase, where an increasingly lower V_{reset} is needed to complete the dissolution of smaller CFs obtained at low I_C (see Figure S3 in the Supporting Information). To account for asymmetric switching, two different activation energies E_{A0} where assumed for set and reset transitions in Equation (2), namely $E_{A0,set} = 0.95$ eV and $E_{A0,reset} = 0.5$ eV, respectively.

The asymmetric switching evidenced by $I_{reset} < I_C$ in Figure 2 can be explained by the effect of the mechanical stress on the CF after the set transition. To evaluate the stress field after set transition, we used a numerical model based on cation migration activated by the electric field and temperature, which was previously adopted to estimate set/reset dynamics in metal oxide nanoionic devices.[33] **Figure 3**a shows the map of calculated impurity concentration n_D [cm^{-3}] in the reset state, obtained by application of a negative voltage to the top electrode. The CF in the reset state shows a depleted gap at the bottom electrode side, as a result of the drift of positively-ionized impurities to the top electrode side during the reset operation. Application of a positive voltage to the top electrode induces set transition, namely migration of cations filling the gap and establishing a continuous CF as shown in Figure 3b. As a result of ion migration, the defect density increases dramatically in the gap region, while it decreases in the CF region which supplied ions during set transition. The density change dictates a local stress σ that can be estimated by:[34]

$$\sigma = K\frac{\Delta n_D}{n} \tag{4}$$

where Δn_D [cm^{-3}] is the local change of n_D due to cation migration, n is the background atomic density of the electrolyte, and $K = E/3(1-2\nu)$ is the bulk modulus, where E is the elastic modulus and ν is the Poisson coefficient. Equation (4) yields a density-driven hydrostatic stress, or pressure, where an increase or a decrease of atomic density leads to a compressive or tensile stress, respectively. Figure 3c shows the map of hydrostatic stress obtained from Equation (4) where Δn_D was given by the difference between the values of n_D in the set state (Figure 3b) and reset state (Figure 3a). In this estimate, the reset state is taken as a reference state with uniform stress, or with small stress gradient compared to the set state. This assumption is justified by the Ag dopant being accumulated at the active-electrode side in the reset state, thus minimizing the compressive stress within the electrolyte. Figure 3d shows the calculated n_D along the symmetry axis y before and after the set transition, while Figure 3e shows the corresponding stress profile. Clearly, the displacement of impurities results in a stress gradient, with compression at the bottom electrode side and tension at the top electrode side. Assuming an impurity concentration in the range of few 10^{21} cm^{-3}, corresponding to a doping level of about 10%, the resulting hydrostatic stress exceeds 1 GPa (i.e., higher than the yield strength of most materials). Note that the local increase of impurities might lead to a general modification of the physical, chemical and transport properties, in addition to the stress gradient. Although these changes might contribute to the observed asymmetric switching, we have restricted our analysis to the stress gradient and its impact on migration in this work. Results similar to Figure 3 would have been obtained in the case of a metallic CF as assumed in Figure 1: in this case, the migration causes an increase in the number of Ag atoms at the bottom electrode side, resulting in a local compressive stress, and a decrease of Ag at the top electrode side, resulting in a local tensile stress (Figure S4 in the Supporting Information). These results demonstrate that relevant stress levels can be achieved by migration of ionized impurities at the nanoscale.

The stress gradient acts as an additional driving force for impurity migration back toward the top electrode, to recover the stress field. This is similar to the phenomenon of wind in the atmosphere, where the wind blows from high-pressure regions to low-pressure regions to react to the pressure difference. Similar migration effects induced by the stress gradient were previously reported for interstitial impurities,[35] vacancies[36] and voids.[37] To illustrate the impact of stress gradient on impurity migration in ECM, **Figure 4**a–c show the energy potential profile for ion migration at $V = V_{set}$ (point P_1 in Figure 4d), $V = V_C$ (bias point P_2) and $V = V_{reset}$ (bias point P_3), respectively. Before CF nucleation at $V = V_{set}$, the energy barrier is $E_{A1} = E_{A0} - \alpha q V_{set}$, in agreement with Equation (1). Nucleation and growth of the CF results in the build-up of a stress field, both in the CF and in the surrounding electrolyte (see Figure 3c). Further ion migration in the direction of the electric field is therefore partially inhibited by the mechanical stress gradient, introducing an elastic potential energy contribution U to the migration barrier. The potential U describes the elastic force driving ions back to the top electrode in response to the stress gradient, similar to a nanoscale wind driving ions from high-pressure regions to low-pressure regions. Note that U is proportional to the stress gradient, namely:

$$U = -\chi\frac{\partial\sigma}{\partial y} \tag{5}$$

where y increases from the bottom to the top electrode as in Figure 3 and $\chi > 0$ is a suitable parameter (see Figure S5 in the Supporting Information). Based on Equation (5), U is zero in case of constant stress (e.g., uniform compressive/tensile or null stress), since the driving force for stress-induced migration would be zero in such case. Although the stress gradient is not uniform along the CF (or, in other words, σ is generally not linear with y), a uniform U was assumed for simplicity.

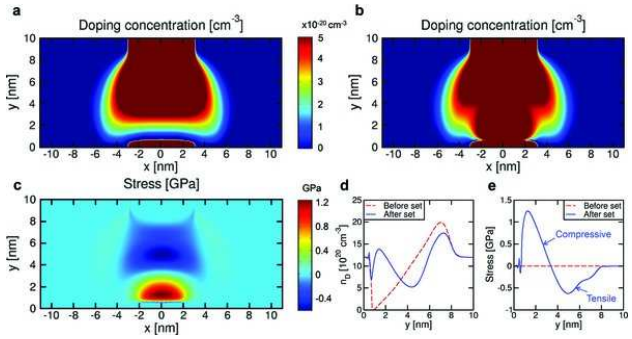

Figure 3. Migration-induced stress field. a,b) Map of defect density in an ECM calculated by a numerical model for ion drift/diffusion activated by field and temperature, for the reset state (a) and the set state (b). The set operation drives the migration of ionized defects from the top reservoir, remaining from the previous reset operation, to the depleted gap at the bottom electrode. The almost continuous CF in the set state (b) accounts for the observed low resistance. c) Map of the hydrostatic component of the stress, obtained from Equation (4). A compressive stress (red) appears close to the bottom electrode, due to the large density increase after ion migration. On the other hand, a tensile stress arises from regions acting as defect reservoir during the set transition. The stress dipole results in an elastic force driving defects from the compressed volume back to the tensed volume, as a reaction to density imbalance. d) Profile of calculated defect density along the vertical axis for the reset state (before set) and for the set state (after set). Due to ion migration, the defect density increases ($\Delta n_D > 0$) close to the bottom electrode and decreases close to the top electrode ($\Delta n_D < 0$). e) Profile of calculated stress along the vertical axis, obtained from Equation (4) in the set and reset state (d). The large stress gradient contributes to defect migration toward the top electrode, thus accounting for asymmetric switching and spontaneous rupture of the CF.

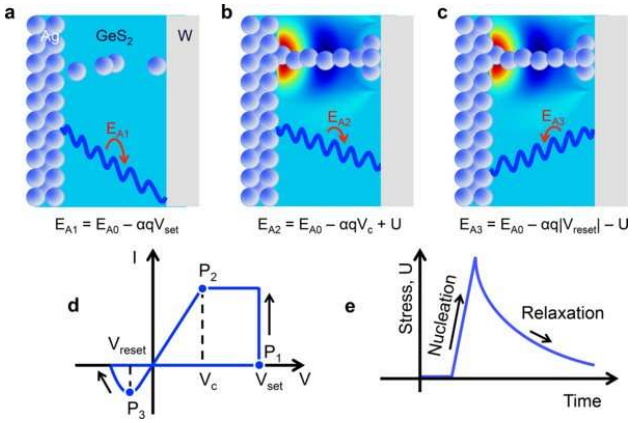

Figure 4. Stress-induced switching asymmetry. a–c) Profile of the potential energy for ion migration within the stress field at the three bias points at V_{set} (point P_1), V_C (P_2) and V_{reset} (P_3) in (d). The colored map in the background indicates the calculated stress field from Figure 3c. Just before the set transition at V_{set} (a, point P_1 in d), the energy barrier is given by Equation (1) with $V = V_{set}$. After CF nucleation and growth at $V = V_C$ (b, point P_2 in d), the elastic potential energy U increases the energy barrier due to the stress gradient, thus partially inhibiting migration in the direction of the electric field. Under negative voltage at $V = V_{reset}$ (c, point P_3 in d), the elastic contribution U decreases the energy barrier, thus accounting for the different energy barriers in the two migration directions. (d) Schematic illustration of the asymmetric I–V curve indicating the three bias points at V_{set} (P_1), V_C (P_2) and V_{reset} (P_3) considered in a, b, c respectively. (e) Schematic illustration of the time evolution of the stress gradient (hence U) in response to cation migration and to the subsequent plastic relaxation of the stress due to viscous flow.

This simplified hypothesis is also in line with the stress profile in Figure 3e, showing a quasi-linear decrease of σ from about $y = 1$ nm to about 5 nm. Thus the barrier for ion migration controlling growth at V_C (bias point P_2) is given by $E_{A2} = E_{A0} - \alpha q V_C + U$ (Figure 4b). Under negative voltage at $V = V_{reset}$ (point P_3), CF dissolution is controlled by ion migration toward the reactive electrode with an energy barrier given by $E_{A3} = E_{A0} - \alpha q|V_{reset}| - U$ (Figure 4c). In this case, the mechanical stress assists ion migration back to the reactive electrode, therefore contributing a negative U to the migration barrier. The activation energy in Equation (2) is thus given by:

$$E_A = E_{A0} - \alpha q V \pm U \quad (6)$$

where the plus/minus sign applies for migration from/to the reactive electrode, respectively, thus accounting for the two different activation energies of set and reset transitions in the calculations of Figure 2. Note that the same activation energy E_{A0} can be assumed for ion migration in the set and reset directions, since the CF shape and size are the same during the final stages of set transition (point P_2, Figure 4b) and the early stages of the reset transition (point P_3, Figure 4c). After the nucleation of the CF and during its growth under an applied voltage, the mechanical stress (hence U) can be released through plastic relaxation, or viscous flow,[38, 39] as described in Figure 4e. This allows to accommodate the growth of the CF by plastic relaxation of the surrounding electrolyte.

The mechanical stress does not only explain the asymmetric migration barriers during set and reset transitions, but also provides a physical interpretation for the dynamic switching effects in **Figure 5**. In these measurements, the ECM device was connected in series with a field-effect transistor (FET) allowing to actively limit the current to below I_C during positive-voltage set. The maximum current I_C was modulated by the transistor gate voltage (see Figure S6 in the Supporting Information), which was kept relatively large ($V_G = 1.5$ V) during the reset operation to ensure a low FET resistance. Figure 5a shows the applied voltage V_A and the measured current I during a typical set/reset measurement: Triangular voltage pulses where used during set and reset with time duration t_{set} and t_{reset}, respectively, separated by a time t_{delay} ($t_{set} = t_{reset} = t_{delay} = 1$ ms in the figure). The current evolution shows an abrupt increase during the positive voltage pulse, marking the set transition, followed

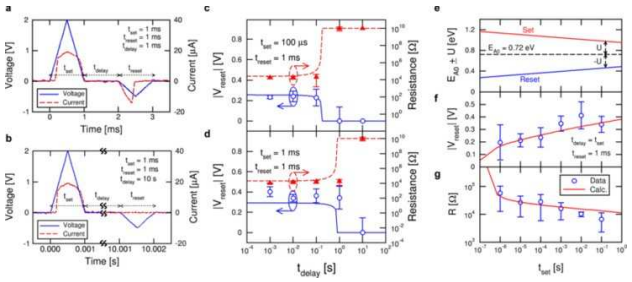

Figure 5. Modeling of CF dissolution and reset. a,b) Measured voltage (blue) and current (red) across the ECM device for a delay time $t_{delay} = 1$ ms (a) and 10 s (b). The device was connected to a FET to limit the current to $I_C = 20$ μA during the set transition. Positive and negative pulses are applied to induce the set and reset transitions, respectively, with pulse duration $t_{set} = t_{reset} = 1$ ms. The absence of a visible reset transition in (b) indicates that the CF already dissolved after 10 s from the set transition, possibly due to the stress field. c,d) Measured and calculated V_{reset} and R as a function of t_{delay}, for $t_{set} = 100$ μs (c) and $t_{set} = 1$ ms (d). Both V_{reset} and the decay time for spontaneous dissolution increase with t_{set}, supporting the relaxation of the stress for increasing set time. e) Energy barriers $E_A = E_{A0} + U$ (set transition) and $E_A = E_{A0} - U$ (reset transition) as a function of t_{set}. The two barriers control ion migration from/to the reactive electrode, respectively. The elastic potential energy U decreases logarithmically with t_{set} as a result of plastic stress relaxation. f,g) Measured and calculated V_{reset} (f) and R (g) as a function of t_{set}. The increase of V_{reset} supports the picture of a time-dependent stress along and nearby the CF. The decrease of R is due to the time-dependent growth of the CF at increasing t_{set}.

by a sudden drop in the negative-voltage pulse, revealing the reset transition (see Figure S7 in the Supporting Information). When the delay time is increased to $t_{delay} = 10$ s in Figure 5b, the current is negligible during the application of the negative pulse, thus evidencing that the CF has already spontaneously dissolved during the delay time. The spontaneous dissolution of the CF can be explained by the elastic contribution U lowering the energy barrier for ion migration back to the reactive electrode, as in Figure 4c. A similar short-term memory effect was previously reported in Cu-based ECM,[27] thus evidencing that the mechanical stress might play a role in other ECM systems too.

Figure 5c shows the evolution of the measured R and V_{reset} with the delay time with $t_{set} = 100$ μs and $t_{reset} = 1$ ms. The resistance was evaluated as the voltage–current ratio along the first part of the negative voltage pulse, while V_{reset} was taken as the applied voltage in correspondence of the reset transition as in Figure 5a (see Figure S7 in the Supporting Information). The resistance first remains constant then sharply rises to a large value for $t_{delay} > 0.1$ s, marking the CF dissolution. The same event is revealed by V_{reset} steeply decreasing to zero for $t_{delay} \approx 1$ s, due to the CF being already dissolved at the time of the negative pulse as in Figure 5b. When the set time is increased to $t_{set} = 1$ ms (Figure 5d), the decay time increases by about an order of magnitude. The impact of t_{set} on the decay time provides evidence for stabilization due to the plastic relaxation in Figure 4e, where a longer set pulse induces a deeper relaxation and thus a smaller U to assist the CF spontaneous dissolution. Calculations are also shown in Figure 5c,d, using Equation (2) with an energy barrier $E_A = E_{A0} - U$ to describe ion migration back to the reactive electrode. The elastic potential energy U was assumed to decrease logarithmically with time as shown by the activation energy for set and reset in Figure 5e, in agreement with the power-law dependence of mechanical and electrical properties during structural relaxation.[39,40]

In addition to the decay time, stress relaxation also impacts V_{reset}, which increases in Figures 5c and d for increasing t_{set} as a result of the smaller U and of the consequently more stable CF. Figure 5f,g show measured and calculated V_{reset} and R, respectively, as a function of t_{set}, for a fixed $t_{reset} = 1$ ms. The delay time was kept equal to t_{set} to ensure that the reset pulse was carried out with a stable CF. The results indicate that V_{reset} increases with t_{set}, which can be explained by the stress relaxation and CF stabilization for increasing t_{set}. Note that viscous flow is strongly accelerated by temperature, therefore it is reasonable to assume that U is a sole function of t_{set} and not of t_{delay}, due to Joule heating causing a large local temperature during set. The decrease of R in Figure 5g can be understood by the CF growth process, which is fully captured by calculations by Equation (2) and (3) with the time-dependent E_A of the set transition in Figure 5e.

These results are consistent with the physical picture of ion migration affected by the mechanical stress and by its logarithmic relaxation with the set time. The different activation energies for migration to/from the reactive electrode are also the origin of the observed asymmetric switching characteristics. It is important to point out that the asymmetric switching cannot be ascribed to the asymmetric ECM structure, where different metals are used for the reactive and the inert electrode. In fact, our results indicate that the switching parameters (e.g., V_{reset} in Figure 5f) are influenced by t_{set}, which rules out that the asymmetric switching can be due to intrinsic material properties, such as the work function. Notably, symmetric switching with $I_{reset} \approx I_C$ was reported for ECM devices based on Ag migration in water electrolyte.[8] These previous results can be understood by the lack of elasticity in liquid water, thus further supporting the role of mechanical stress in the asymmetric ECM switching. On the other hand, resistance switching in valence-change memories based on metal oxides such as HfO_x (ref. [30,33]) and TaO_x (ref. [41] displays symmetric behavior with $|V_{reset}| = V_C$ and $I_{reset} = I_C$.[30,31] This might be because both cations (e.g., Hf^+ in HfO_x) and anions (O^{2-}) are available to migrate into opposite directions, thus allowing for a redistribution of different species and avoiding the buildup of stress gradients. The absence of a significant migration-induced stress gradient explains the substantial symmetry of resistance switching characteristics in metal oxides.

An asymmetric shape of the CF would also not account for the asymmetric switching. Although a cylindrical filament was used here for simplicity, other works have speculated about the possible conical shape of the CF,[6,24] or about the presence of a significant gap resulting in an asymmetric structure of the

CF.[32] An asymmetric CF, however, is expected to yield polarity independent microscopic parameters, such as temperature and electric field which act as driving force for migration. The energy barrier for ion migration is also expected to be the same irrespective of the voltage polarity, even for a cone-shaped or an interrupted CF. Therefore, an asymmetric shape of the CF would not account for the observed difference in switching voltages for positive and negative bias, namely V_C and V_{reset} respectively. Note that V_C and V_{reset} refer to the same CF state, namely the one obtained at the end of the set transition, although under different voltage polarity. Similarly, an asymmetric CF due to different interface resistance at the top and bottom electrodes would not account for the observed asymmetric switching behavior, since the potential profile is not expected to depend on the applied voltage polarity.

Other potential sources of switching asymmetry can be similarly ruled out. Diffusion, for instance, might contribute a directional driving force for migration, as a result of the directional concentration gradient. However, diffusion during the reset transition induces migration toward the bottom electrode, thus opposite to the reset process. This is because the reset migration increases the defect concentration at the top electrode side and decreases the concentration at the bottom electrode side (see Figure S8 in the Supporting Information). The concentration gradient across the resulting accumulated/depleted regions drives diffusion toward the bottom electrode, thus competing with drift-induced migration toward the top electrode. Electromigration due to the momentum transfer from electrons to atoms in the CF also cannot account for switching asymmetry, since this effect is equally present during set and reset processes. In fact, electromigration would cause defect migration toward the top electrode during set and toward the bottom electrode during reset, thus opposite to the ion migration and unable to account for any switching asymmetry.

Electrostatic polarization effects cannot account for the observed asymmetric switching and spontaneous rupture of the CF. After set transition, a positive charge might accumulate at the bottom-electrode side, due to polarization of the insulating electrolyte. This hypothetical accumulated charge would be detected as a non-zero crossing of the *I*–*V* curve in the set state, which however is generally not seen. This was explained by the presence of the CF providing a short-circuit path to readily discharge any accumulated charge.[42] Charge polarization must therefore be ruled out as a possible cause of asymmetric switching in ECM.

Size-dependent dissolution of the CF might arise because of the low dimensionality of the CF. [43] For instance, the melting point of metallic nanoparticles was shown to decrease for decreasing particle size due to the large surface-to-volume ratio.[44–47] This might contribute to switching asymmetry, because Ag atoms in the CF would be relatively unstable with respect to the almost bulk-like Ag electrode, thus resulting in a negative difference ΔG of the Gibbs free energy for the transfer of Ag from the filament to the top electrode, hence in a lower driving force needed to transfer Ag from the CF to the electrode during the reset operation. On the other hand, size-dependent dissolution could hardly explain the impact of t_{set} on CF stability and V_{reset} in Figure 5, since the thermodynamic stability of the CF at a given size in the reset process should not change with annealing conditions in the previous set process. However, the impact of size-dependent dissolution on switching asymmetry cannot be ruled out. Similarly, chemical reactions such as the formation of compounds made of Ag, Ge and S might also depend on voltage polarity, thus possibly contribute to the asymmetric switching.

As previously mentioned, the ionic transport properties might also depend on the local composition of impurities close to the CF. In case of a significant dependence of E_A on the Ag concentration, for instance, a directional force might arise contributing to the observed asymmetric switching. Further studies are needed to assess the impact of Ag concentration on transport properties and the corresponding impact on switching asymmetry in GeS_2.

In summary, we have provided evidence for asymmetric switching in ECM devices. We have shown that asymmetric switching can be explained by the mechanical compressive stress induced by the CF growth. The stress differently affects ion hopping in the two migration directions, therefore leading to switching asymmetry and even spontaneous CF dissolution. These effects are modulated by the duration of the set pulse through plastic stress relaxation due to the viscous flow, as evidenced by time-dependent CF stability and reset voltage. The role of other effects (diffusion, electromigration, etc.) have been discussed, highlighting the possible contribution of size-dependent dissolution to switching asymmetry and of the change of material properties (e.g., chemical potential and transport properties) due to local concentration of impurities in the CF. Our results provide new directions for improving ECM reliability and switching through control of the stress around the CF either through electrolyte engineering or stress-aware programming schemes.

Experimental Section

Devices: The ECM device used in this study consists of a two-terminal resistor-type device with a top reactive electrode (Ag), a bottom inert electrode (W) and a chalcogenide glass (GeS_2) as the solid-state electrolyte between the electrodes. The Ag/GeS_2/W stack was fabricated in the back-end of the line on a Si substrate. The W bottom electrode was defined by conventional photolithography and had a size of 0.2 μm. The solid-state electrolyte was obtained by PVD process and has a thickness of 50 nm. The electrolyte was doped by Ag through deposition of a thin Ag layer and photo-diffusion process. The doping level evaluated by secondary ion mass spectroscopy (SIMS) was 4×10^{18} cm^{-3}, thus significantly lower than the local doping needed to activate local conduction in the set state, which explains the initial high resistance (> 10 GΩ) of our ECM devices. The top Ag electrode was deposited and protected by TiN as a diffusion barrier. Metal lines and contact pads where finally deposited and patterned by lithography for the purpose of electrical characterization. In some of the structures studied in this work, the ECM was connected to an n-type FET with channel width and length $W = 0.5$ μm and $L = 0.14$ μm, fabricated by standard CMOS flow in an industrial process line. In

these structures, the drain of the transistor was connected to the W contact of the ECM by a metal via. Gate and source terminals of the FET were connected to pad contacts for electrical characterization.

Characterization. The dc conduction characteristic of ECM were collected by an Agilent B1500A Semiconductor Parameter Analyzer connected to the experimental device within a conventional probe station for electrical characterization. The current during the set transition was limited to a value I_C by using the compliance mode of the Agilent B1500A, or by properly biasing the gate voltage in the FET in series with the ECM device. Time-resolved analysis was achieved by application of pulses by a TTi – TGA 12102 arbitrary waveform generator with a 100 MHz bandwidth to deliver rectangular and triangular pulses. The applied voltage was captured by an active probe connected to a Lecroy Waverunner oscilloscope with 600 MHz bandwidth and maximum 10 Gsample/s sampling rate. The current response of the ECM was collected by feeding it into the 50-Ω input of the oscilloscope and collecting the resulting voltage waveform.

Numerical Calculations. DC switching characteristics were calculated by assuming an increasing voltage sweep of positive/negative sign for set/reset transitions, respectively. The CF diameter was calculated through Equation (1)–(3), previously applied to the nanoionic switching in metal oxides,[30] thus allowing the calculation of the ECM resistance, hence of the current flowing through the device. During reset, the same Equation (2) was used, except for an opposite sign of the pre-exponential factor *A*. The mechanical stress was evaluated by numerical simulations of ion migration through drift and diffusion activated by the electric field and the temperature.[33] In the numerical simulations, the diffusivity D was calculated by the Arrhenius formula, namely $D = D_0\exp(E_D/kT)$, where $D_0 = 2 \times 10^{-3}$ cm^2 s^{-1} is the pre-exponential constant, $E_D = 1$ eV is the activation energy and T is the local temperature.[33] From the density change Δn_D, the stress was calculated by Equation (4) using reported mechanical properties of Ge_3Se_7, (similar to the chalcogenide GeS_2 used in our work), namely $E = 17.9$ GPa and $\nu = 0.264$.[43] Time-resolved characteristics were calculated by Equation (2) and (6), where U was assumed to change with time according to the logarithmic evolution in Figure 5e. This method allowed the calculation of the decay time for $V = 0$ and of the reset voltage V_{reset}, as the voltage to initiate the CF dissolution along a voltage triangular pulse.

Supporting Information

Supporting Information is available from the Wiley Online Library or from the author.

Acknowledgements

This work was supported in part by Fondazione Cariplo (grant number 2010–0500).

[1] R. Waser, M. Aono, *Nat. Mater.* **2007**, *6*, 833.
[2] R. Waser, R. Dittmann, G. Staikov, K. Szot, *Adv. Mater.* **2009**, *21*, 2632.
[3] C. Schindler, M. Weides, M. N. Kozicki, R. Waser, *Appl. Phys. Lett.* **2008**, *92*, 122910.
[4] K. Terabe, T. Hasegawa, T. Nakayama, M. Aono, *Nature* **2005**, *433*, 47.
[5] M. N. Kozicki, M. Park, M. Mitkova, *IEEE Trans. Nanotechnology* **2005**, *4*, 331.
[6] U. Russo, D. Kalamanathan, D. Ielmini, A. L. Lacaita, M. N. Kozicki, *IEEE Trans. Electron Devices* **2009**, *56*, 1040.
[7] D.-Y. Cho, I. Valov, J. van der Hurk, S. Tappertzhofen, R. Waser, *Adv. Mater.* **2012**, *24*, 4552.
[8] X. Guo, C. Schindler, S. Menzel, R. Waser, *Appl. Phys. Lett.* **2007**, *91*, 133513.
[9] J. R. Jameson, N. Gilbert, F. Koushan, J. Saenz, J. Wang, S. Hollmer, M. N. Kozicki, *Appl. Phys. Lett.* **2011**, *99*, 063506.
[10] Z. Xu, Y. Bando, W. Wang, X. Bai, D. Golberg, *ACS Nano* **2010**, *4*, 2515.
[11] S.-J. Choi, G.-S. Park, K.-H. Kim, S. Cho, W.-Y. Yang, X.-S. Li, J.-H. Moon, K.-J. Lee, K. Kim, *Adv. Mater.* **2011**, *23*, 3272.
[12] Y. Yang, P. Gao, S. Gaba, T. Chang, X. Pan, W. Lu, *Nat. Commun.* **2012**, *3*, 732.
[13] Q. Liu, J. Sun, H. Lv, S. Long, K. Yin, N. Wan, Y. Li, L. Sun, M. Liu, *Adv. Mater.* **2012**, *24*, 1844.
[14] I. Valov, R. Waser, J. R. Jameson, M. N. Kozicki, *Nanotechnology* **2011**, *22*, 254003.
[15] C. Gopalan, Y. Ma, T. Gallo, J. Wang, E. Runnion, J. Saenz, F. Koushan, P. Blanchard, S. Hollmer, *Solid-State Electronics* **2011**, *58*, 54.
[16] T. Sakamoto, H. Sunamura, H. Kawaura, T. Hasegawa, T. Nakayama, M. Aono, *Appl. Phys. Lett.* **2003**, *82*, 3032.
[17] X. F. Liang, Y. Chen, L. Shi, J. Lin, J. Yin, Z. G. Liu, *J. Phys. D: Appl. Phys.* **2007**, *40*, 4767.
[18] S. Tappertzhofen, I. Valov, R. Waser, *Nanotechnology* **2012**, *23*, 145703
[19] Y. Cho, S. Tappertzhofen, R. Waser, I. Valov, *Sci. Rep.* **2013**, *3*, 1169.
[20] Y. Dong, G. Yu, M. C. McAlpine, W. Lu, C. M. Lieber, *Nano Lett.* **2008**, *8*, 386.
[21] M. N. Kozicki, C. Gopalan, M. Balakrishnan, M. Mitkova, *IEEE Trans. Nanotechnology* **2006**, *5*, 535.
[22] T. Sakamoto, M. Tada, K. Okamoto, H. Hada, *IEEE Trans. Electron Devices* **2012**, *59*, 3574.
[23] S. Kaeriyama, T. Sakamoto, H. Sunamura, M. Mizuno, H. Kawaura, T. Hasegawa, K. Terabe, T. Nakayama, M. Aono, *IEEE J. Solid-State Circuits* **2005**, *40*, 168.
[24] S. Yu, H.-S. P. Wong, *IEEE Int. Electron Devices Meeting (IEDM)* **2010**, 520.
[25] T. Ohno, T. Hasegawa, T. Tsuruoka, K. Terabe, J. K. Gimzewski, M. Aono, *Nat. Mater.* **2011**, *10*, 591.
[26] J. Park, S. Jung, W. Lee, S. Kim, J. Shin, D. Lee, J. Woo, H. Hwang, *IEEE Electron Device Lett.* **2012**, *33*, 646.
[27] T. Liu, M. Verma, Y. Kang, M. Orlowski, *Appl. Phys. Lett.* **2012**, *101*, 073510.
[28] R. Soni, P. Meuffels, G. Staikov, R. Weng, C. Kügeler, A. Petraru, M. Hambe, R. Waser, H. Kohlstedt, *J. Appl. Phys.* **2011**, *110*, 054509.

[29] I. Valov, I. Sapezanskaia, A. Nayak, T. Tsuruoka, T. Bredow, T. Hasegawa, G. Staikov, M. Aono, R. Waser, *Nat. Mater.* **2012**, *11*, 530.
[30] D. Ielmini, *IEEE Trans. Electron Devices* **2011**, *58*, 4309.
[31] D. Ielmini, F. Nardi, C. Cagli, *IEEE Trans. Electron Devices* **2011**, *58*, 3246.
[32] S. Menzel, U. Böttger, R. Waser, *J. Appl. Phys.* **2012**, *111*, 014501.
[33] S. Larentis, F. Nardi, S. Balatti, D. C. Gilmer, D. Ielmini, *IEEE Trans. Electron Devices* **2012**, *59*, 2468.
[34] D. Halliday, R. Resnick, K. S. Krane, *Physics*, Vol. *1*, 4th edition, Wiley, New York **1992**.
[35] V. V. Kirsanov, S. B. Kislitsin, E. M. Kislitsina, *Phys. Status Solidi A* **1984**, *86*, 199.
[36] D. L. Olmsted, R. Phillips, W. A. Curtin, *Modell. Simul. Mater. Sci. Eng.* **2004**, *12*, 781.
[37] T. O. Ogurtani, O. Akyildiz, *J. Appl. Phys.* **2008**, *104*, 023521.
[38] J. Kalb, F. Spaepen, T. P. Leervad Pedersen, M. Wuttig, *J. Appl. Phys.* **2003**, *94*, 4908.
[39] J.-P- Guin, T. Rouxel, V. Keryvin, J.-C. Sangleboeuf, I. Serre, J. Lucas, *J. Non-Cryst. Solids* **2002**, *298*, 260.
[40] D. Ielmini, S. Lavizzari, D. Sharma, A. L. Lacaita, *Appl. Phys. Lett.* **2008**, *92*, 193511.
[41] M.-J. Lee, C. B. Lee, D. Lee, S. R. Lee, M. Chang, J. H. Hur, Y.-B. Kim, C.-J. Kim, D. H. Seo, S. Seo, U-I. Chung, I.-K. Yoo, K. Kim, *Nat. Mater.* **2011**, *10*, 625.
[42] I. Valov, E. Linn, S. Tappertzhofen, S. Schmelzer, J. van den Hurk, F. Lentz, R. Waser, *Nat. Commun.* **2013**, *4*, 1771.
[43] Y. Gueguen, T. Rouxel, P. Gadaud, C. Bernard, V. Keryvin, J.-C. Sangleboeuf, *Phys. Rev. B* **2011**, *84*, 064201.
[44] D. Ielmini, *IEDM Tech. Dig.* **2011**, 409.
[45] M. Takagi, *J. Phys. Soc. Jpn.* **1954**, *9*, 359.
[46] S. L. Lai, J. Y. Guo, V. Petrova, G. Ramanath, L. H. Allen, *Phys. Rev. Lett.* **1996**, *77*, 99.
[47] H. Sakai, *Surf. Sci.* **1996**, *351*, 285.
[48] K. K. Nanda, S. N. Sahu, S. N. Behera, *Phys. Rev. A* **2002**, *66*, 013208.